The dark side of zircon: textural, age, oxygen isotopic and trace element evidence of fluid saturation in the subvolcanic reservoir of the Island Park-Mount Jackson Rhyolite, Yellowstone (USA)

Author(s):
Troch, Juliana; Ellis, Ben S.; Schmitt, Axel K.; Bouvier, Anne-Sophie; Bachmann, Olivier

Publication date:
2018-07

Permanent link:
https://doi.org/10.3929/ethz-b-000271924

Originally published in:
Contributions to Mineralogy and Petrology 173(7), https://doi.org/10.1007/s00410-018-1481-2

Funding acknowledgement:
ETH-05 13-2 - Petrogenesis of low d180 rhyolites in the Snare River Plain - Yellowstone area, Western USA: a geochemical and experimental approach (ETHZ)

Contributions to Mineralogy and Petrology (2018) 173:54
https://doi.org/10.1007/s00410-018-1481-2

ORIGINAL PAPER

The dark side of zircon: textural, age, oxygen isotopic and trace element evidence of fluid saturation in the subvolcanic reservoir of the Island Park-Mount Jackson Rhyolite, Yellowstone (USA)

Juliana Troch[1] · Ben S. Ellis[1] · Axel K. Schmitt[2] · Anne-Sophie Bouvier[3] · Olivier Bachmann[1]

Received: 9 March 2018 / Accepted: 11 June 2018 / Published online: 16 June 2018

Abstract

The Island Park-Mount Jackson series in the Yellowstone volcanic field, Wyoming (USA), is a suite of rhyolitic domes and lavas that erupted between the caldera-forming eruptions of the Mesa Fall Tuff (1.3 Ma) and the Lava Creek Tuff (0.6 Ma). Combined zircon U/Pb geochronology, Raman spectroscopy, oxygen isotopic and trace elemental compositions document storage conditions of these magmas between consecutive supereruptions. Based on comparison with co-erupted melt compositions and textural criteria, four zircon compositional groups are identified that record different stages along a continuous magmatic evolution from trace element-poor rhyolite at high temperatures to extremely fractionated rhyolite where zircon trace elements are highly enriched (e.g., > 1000 ppm U). These latter zircon domains are dark in cathodoluminescence images and show broadened Raman peaks relative to near-endmember zircon, indicating that substitution of non-stoichiometric trace elements into zircon leads to distortion of the crystal lattice. Some of these zircon domains contain inclusions of U-Th-REE-phases, likely originating from coupled dissolution–reprecipitation of metastable trace element-rich zircon in the presence of a fluid phase. Rhyolite-MELTS simulations indicate that at the conditions required to produce the observed enrichment in trace elements, a fluid phase is likely present. These findings illustrate that zircons can be assembled from a variety of co-existing magmatic environments in the same magma reservoir, including near-solidus volatile-rich melts close to the magmatic–hydrothermal transition.

Keywords Rhyolite · Yellowstone · Zircon · Magmatic–hydrothermal · Near-solidus

Introduction

High-silica rhyolite magmas have produced some of the largest volcanic eruptions throughout the Earth's history, with consequences ranging from regional landscape destruction to global climate alteration (e.g., Robock 2002). The geothermally hyperactive Yellowstone volcanic field (Wyoming/USA) has produced three caldera-forming eruptions in the past 2 million years from a magma reservoir that was intermittently sampled by smaller-scale effusive domes and lava flows. Despite the far-reaching impact of these eruptions, no consensus exists about the storage conditions at which large volumes of high-silica rhyolite magma are accumulated in the Earth's crust, with some researchers advocating long-term "warm storage" at near-solidus temperatures (> 700 °C; Barboni et al. 2016; Szymanowski et al. 2017), while others favour rapid remobilisation from immobile or even subsolidus "cold storage" conditions (Cooper and Kent 2014; Rubin et al. 2017).

Communicated by Othmar Müntener.

Electronic supplementary material The online version of this article (https://doi.org/10.1007/s00410-018-1481-2) contains supplementary material, which is available to authorized users.

✉ Juliana Troch
juliana.troch@erdw.ethz.ch

[1] Institute of Geochemistry and Petrology, ETH Zurich, Clausiusstrasse 25, 8092 Zurich, Switzerland

[2] Institut für Geowissenschaften, Universität Heidelberg, Im Neuenheimer Feld 236, 69120 Heidelberg, Germany

[3] Institute of Earth Sciences, Université de Lausanne, Géopolis, 1015 Lausanne, Switzerland

Zircons are powerful geochronometers, as their textural, trace elemental and isotopic compositions preserve information both about the timing of crystallisation and the composition and temperature of their host melt; additionally, their resistance to alteration and dissolution allows them to reliably record the thermochemical evolution in magmas over extensive time periods, whereas this information is usually obliterated in cogenetic melt or mineral phases. In this study, we analysed zircons from the Island Park-Mount Jackson Rhyolite series, a suite of lavas erupted prior to the 1000 km^3 eruption of the Lava Creek Tuff at 0.63 Ma, which uniquely records conditions between two supervolcanic events. Textural observations are combined with age and oxygen isotopic data, trace element models, Ti-in-zircon thermometry and rhyolite-MELTS models, to document different storage conditions of rhyolite magma in Yellowstone prior to its youngest supereruption—a state within the Yellowstone system that may resemble its current condition.

Geological background

Silicic volcanism in the Yellowstone volcanic field has resulted in three caldera-forming eruptions, which have produced the Huckleberry Ridge Tuff (HRT 2.1 Ma, Rivera et al. 2014), Mesa Falls Tuff (MFT 1.3 Ma, Ellis et al. 2017; Rivera et al. 2016) and the Lava Creek Tuff (LCT 0.6 Ma, Matthews et al. 2015; Wotzlaw et al. 2015). The Island Park member (IP) consists of five small-volume rhyolitic domes that erupted in the area of the MFT-related Henry's Fork caldera closely after the caldera-forming eruption of the MFT (Christiansen 2001; Stelten et al. 2017; Troch et al. 2017). The rhyolitic lava flows of the Mount Jackson member (MJ) are considered pre-caldera units of the following caldera-forming LCT eruption, with the petrologically distinct Lewis Canyon Rhyolite erupted within the MJ member (Table 1). Temporal overlap between Ar–Ar ages of the MJ units with the IP member suggests that magmatic activity between the MFT and LCT caldera-forming eruptions occurred in discrete clusters of contemporaneous lava flows erupted over a wide area (Troch et al. 2017).

All units of the Island Park-Mount Jackson rhyolite series (IPMJ) are high-silica rhyolites (> 75 wt% SiO_2) with abundant sanidine and quartz occurring in mm-sized crystals. Additional minerals include plagioclase, clino- and orthopyroxene, hornblende, fayalite and accessory zircon, apatite, allanite and chevkinite. In contrast to the other units, the Lewis Canyon Rhyolite contains abundant plagioclase. The IPMJ units have been characterised in detail in Troch et al. (2017); here we focus on the zircon record of a subset of these units, namely Osbourne Butte (OB) and Silver Lake dome (SL) from the IP member, the transitional unit Moose Creek flow (MC) and the youngest unit Mt. Haynes Rhyolite (MH, both MJ), as well as the Lewis Canyon Rhyolite (LC).

Table 1 Effusive units erupted between Mesa Falls Tuff (1.3 Ma) and Lava Creek Tuff (0.63 Ma); units in bold are investigated in this study

Member	Unit	Abbr.	$^{40}Ar/^{39}Ar$ age (Ma)[a]	Other ages	$^{206}Pb/^{238}U$ (Ma)[e]	MSWD	*n*
Island Park domes (IP)	Warm River Butte	WR	1.2943 ± 0.0026	1.2880 ± 0.0043[b]			
	Silver Lake dome	SL	1.2839 ± 0.0114	1.2887 ± 0.0020[b]	1.32 ± 0.14	0.85	9
	Osbourne Butte	OB	1.2784 ± 0.0054	1.2921 ± 0.0016[b]	1.25 ± 0.10	1.51	11
	Elk Butte	EB	1.2777 ± 0.0092	1.2897 ± 0.0018[b]			
	Lookout Butte	LB	1.2190 ± 0.0146	1.2912 ± 0.0021[b]			
Mount Jackson Rhyolite (MJ)	**Moose Creek flow**	MC	1.2856 ± 0.0066	1.22 ± 0.02[c]	1.40 ± 0.08	0.47	11
	Wapiti Lake flow	WL	1.2187 ± 0.0160	1.16 ± 0.02[c]			
	Flat Mountain Rhyolite	FM		0.929 ± 0.068[c]			
	Harlequin Lake flow	HL	0.8300 ± 0.0074	0.839 ± 0.016[c]			
	Big Bear Lake flow	BB		> 0.64, < 0.78[d]			
	Mt. Haynes Rhyolite	MH	0.7016 ± 0.0016	0.609 ± 0.012[c]	0.835 ± 0.072	1.19	10
Lewis C. Rh	**Lewis Canyon Rhyolite**	LC	0.8263 ± 0.0186	0.853 ± 0.014[c]	0.98 ± 0.12	0.55	12

[a] $^{40}Ar/^{39}Ar$ age on sanidine, uncertainty is full external precision 2σ (Troch et al. 2017)

[b] $^{40}Ar/^{39}Ar$ age ± 2σ on sanidine (Stelten et al. 2017)

[c] K/Ar ages ± 2σ on sanidine (Obradovich 1992) as reported in Christiansen (2001)

[d] Age constraint based on stratigraphy (Christiansen 2001)

[e] This study; based on average rim analyses on cross-sectioned zircon crystals where analysis points do not overlap with CG-4 zircon cores. Uncertainty is 2 SE. Analyses considered are marked in bold in suppl. Table 1

Methods

Preparation and electron microscopy

Following crushing using the Selfrag electric pulse disaggregation apparatus at ETH Zurich, zircons were separated from the sieved < 710 µm fraction of rhyolite lava samples described in detail in Troch et al. (2017) by standard density (sodium polytungstate) and magnetic separation techniques. Together with the three zircon standard reference materials Penglai, 91500 and Temora 2, sample zircon crystals were mounted in Specifix-20 epoxy and polished. To avoid beam damage, detailed imaging (Fig. 1) with secondary electron (SE), backscatter electron (BSE) and cathodoluminescence (CL) images and inclusion identification was carried out after ion probe analytical work on the slightly repolished and carbon-coated epoxy mount. Imaging and inclusion identification by energy-dispersive X-ray spectrometry (EDS) were performed with a JEOL JSM-6390 LA scanning electron microscope equipped with a Thermo Fisher NORAN NSS7 EDS system with a 30 mm^2 silicon-drift detector at ETH Zurich. Additional wavelength-dispersive X-ray spectrometry (WDS) scans by electron microprobe were used to confirm the results for mineral inclusion identification (suppl. Table 6). Photomicrographs were taken under an optical microscope.

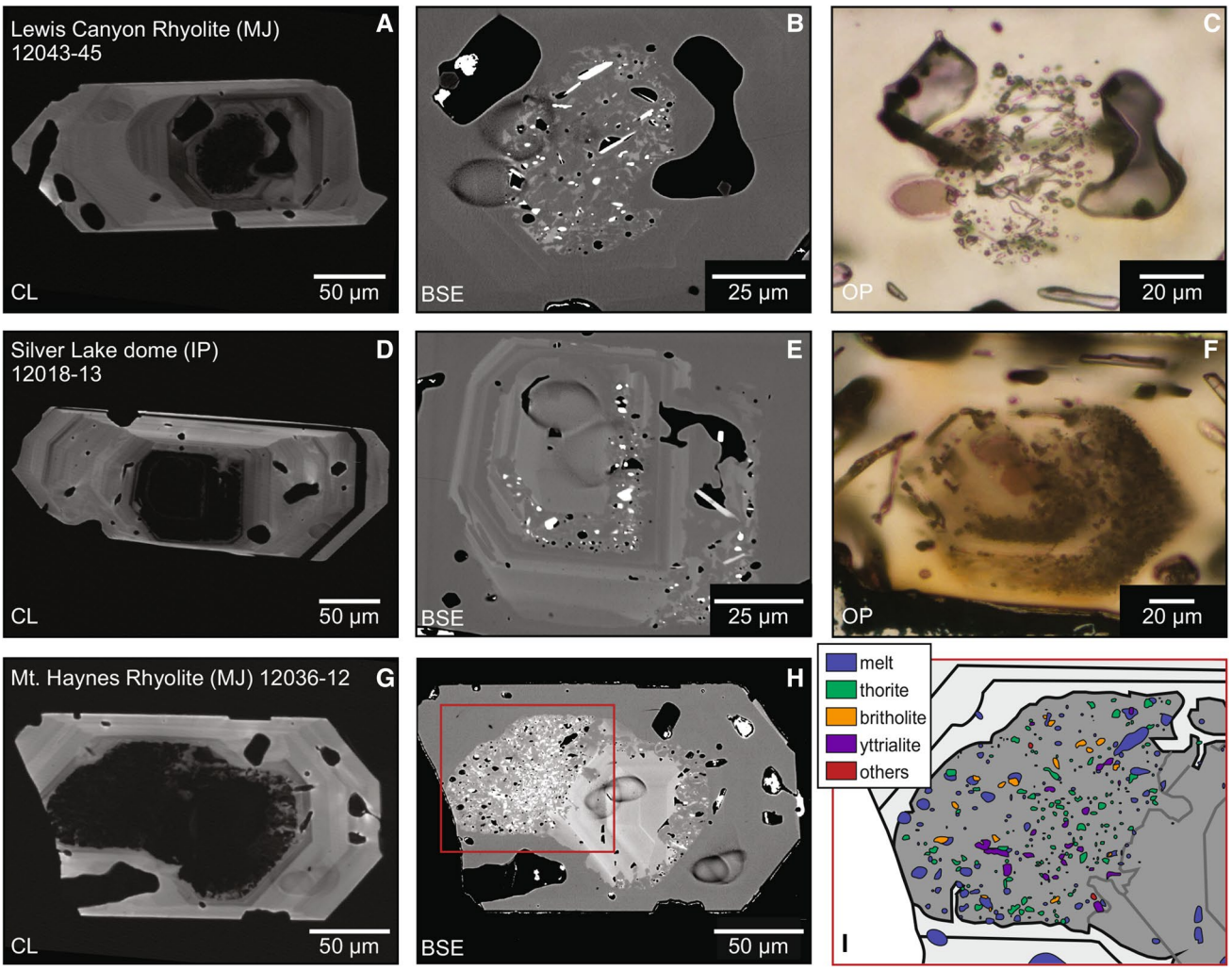

Fig. 1 Images of zircons with CL-dark cores by cathodoluminescence (CL, first column, panels **a**, **d**, **g**), backscattered electron imaging (BSE, second column, panels **b**, **e**, **h**), and optical microscopy (**c, f**). Sketch in K illustrates the distribution of U-Th-REE-rich accessory phases in the dark-CL core as identified by EDS. Note that a clear distinction between melt inclusions and holes (previously fluid-filled?) is difficult. The different shape of the inclusion-rich zones in **f** compared to **e** is related to crystal sectioning effects

Secondary ion mass spectrometry

Single crystal core and rim oxygen isotope analyses on zircons were measured via secondary ion mass spectrometry (SIMS) with a CAMECA ims 1280-HR ion microprobe at the Institute of Earth Sciences at the University of Lausanne. A 10 kV Cs^+ primary beam was employed with a current of ~ 2 nA, resulting in a ~ 10 µm beam size. The electron flood gun with normal incidence was used to compensate charging. ^{16}O and ^{18}O negative secondary ions were extracted at 10 kV and a mass resolution power of $m/\Delta m = 2400$ and collected on Faraday cups in multi-collection mode. Faraday cups were calibrated at the beginning of the session, and mass calibration was performed every 12 h. Each analysis took ca. 4 min, including pre-sputtering (30 s) and automated centering of secondary electrons, followed by integration of secondary ion counts. Reproducibility was 0.32‰ (2 standard deviations, SD) on Penglai zircon used as a primary standard (Li et al. 2010) during the session. Internal measurement uncertainties for individual analyses were usually ≤ 0.2‰ (2 standard error, SE). The error reported for all samples reflects the 2 SD calculated from bracketing analyses of the reference zircon. Zircon reference materials 91500 (Wiedenbeck et al. 2004) and Temora 2 (Black et al. 2004) were measured intermittently during the session as checks for accuracy and precision (both $n = 4$, suppl. Table 3). Variability of the 91500 results is similar to the overall reproducibility of Penglai, while the larger variability of Temora 2 zircons (0.47‰, 2 SD) suggests that the selected Temora 2 zircon grains were slightly less homogeneous. Instrumental mass fractionation factors determined from Penglai were applied to Temora 2 and 91500 zircons, resulting in average values of 8.39 ± 0.47 and 10.40 ± 0.29‰, respectively, within uncertainty of the published values of 8.2 ± 0.1 and 9.9 ± 0.3‰ (Black et al. 2004; Wiedenbeck et al. 2004).

U-Pb dating of zircons was carried out via SIMS at the Institut für Geowissenschaften, Universität Heidelberg, using a CAMECA ims 1280-HR ion microprobe. A mass-filtered $^{16}O^-$ primary beam with an intensity of 15–20 nA was focused to a size of 25–30 µm. Secondary ions were extracted at 10 kV, a mass resolution power $m/\Delta m = 4500$ at 10% of the peak height, and an energy bandpass of 50 eV. Reference zircon Temora 2 (Black et al. 2004) was used as a primary standard during calibration, using a UO_2/U vs. Pb/U relative sensitivity calibration. Variability of the ^{204}Pb-corrected $^{206}Pb/^{238}U$ age for Temora 2 was 3.2% (2 SD). 91500 (1065 Ma; Wiedenbeck et al. 1995) and Penglai (4.4 Ma; Li et al. 2010) reference zircon were analysed intermittently as secondary references (91500 $n = 5$; Penglai $n = 14$, suppl. Table 2). The ^{207}Pb-corrected (assuming common $^{207}Pb/^{206}Pb = 0.8283$) $^{206}Pb/^{238}U$ ages for 91500 and Penglai agree within − 2.7 and − 0.9% with reported values, respectively. The $^{206}Pb/^{238}U$ ages for unknowns were also corrected for common Pb using common $^{207}Pb/^{206}Pb = 0.8283$. In addition, an age correction for initial ^{230}Th deficit was applied based on the calculated partitioning from measured Th/U in zircon and Th/U in the melt, which was determined from glass analyses from two of the IPMJ units (Troch et al. 2017).

Trace element analyses via SIMS at Heidelberg were obtained from the same growth zones as previous oxygen isotope and U-Pb analyses, using a ~ 15–20 nA $^{16}O^-$ primary ion beam. High energy (+ 100 eV) secondary ions were analysed at intermediate mass resolution ($m/\Delta m = 2000$) using energy-filtering to suppress molecular interferences. Remaining oxide interferences were subtracted using atomic to oxide ratios determined from analysis of synthetic glasses selectively doped with rare earth elements (REE) to generate interference-free patterns. Trace element relative sensitivity factors were calibrated using NIST SRM 610 glass (Pearce et al. 1997) with a reproducibility of < 4% (2 SD) for REE, U, Th, Y. Masses ^{26}Mg and ^{57}Fe were analysed to monitor for potential beam overlap onto non-zircon inclusions. Reference zircon 91500 was used to monitor accuracy of the relative sensitivity calibration ($n = 8$, suppl. Table 3).

Electron microprobe analyses

Trace element profiles were measured on a JEOL JXA-8200 Electron Probe Microanalyser (EPMA) at ETH Zurich at 20 kV, 180 nA and 2 µm beam diameter. Counting times were 600 s on the peak and 300 s on the background for P Kα, Al Kα, Y Lα; 360 s/180 s for U $M\beta_1$ and Th $M\alpha_1$, 300 s/150 s for Dy Lß and Er Lα, 150 s/75 s for Hf Lα and 20 s/10 s for Zr Lα and Si Lα. Peaks were selected following detailed intensity scans on samples and backgrounds adjusted for calibration on high-concentration reference materials where required. Reference materials were zircon (Si, Zr), corundum (Al), elemental hafnium (Hf), thorianite (Th), uraninite (U), synthetic YAG-crystal (Y), as well as synthetic $DyAlO_3$ (Dy) and $ErAlO_3$ (Er). U contents were corrected for interference with Th Mα (Åmli and Griffin 1975) and Hf for interference with Er. Due to a lack of zircon reference materials with similarly high trace element contents, previously acquired SIMS results on the same growth zones were used to verify electron microprobe data and are plotted together where EPMA data are shown.

Raman spectroscopy

Raman spectra were collected for all zircons on the same growth zone as SIMS trace element analyses with a DILOR Labram micro-Raman spectrometer equipped with an Olympus microscope and an external Ar-ion laser at ETH Zurich. An exciting wavelength of 532.11 nm was used, the hole width was set to 600 µm and the slit

to 300 µm with a gritting of 1800. Output power on the sample was 12 mW at 20% laser power. At least three spots were analysed for each growth zone and each Raman spectrum was acquired for 3 s over two accumulations at a magnification of 1000×. All spectra were calibrated against a silicon wafer peak at 520.6 cm^{-1} and reduced by automated, iterative curve fitting with the software IFORS (Lünsdorf and Lünsdorf 2016) to standardise the fitting procedure.

Results

Zircon textures

Zircons in the IPMJ lavas comprise mostly euhedral prismatic elongate grains that commonly display oscillatory zoning and minor sector zoning. About 70% of all grains contain inclusions, mostly apatite and melt inclusions, which may contain small vapour bubbles. All units include grains with dark-CL zones (mostly cores) with indistinct rims and higher backscatter intensities (Fig. 1, 4–16% of grains in each unit). These dark-CL zircon domains have been described for several other units in Yellowstone, such as the post-LCT lavas (Bindeman et al. 2008), MFT (Rivera et al. 2016) and LCT members A and B (Matthews et al. 2015). While they have not been described explicitly for HRT, CL images in Rivera et al. (2014) clearly show several dark-core zircons among the analysed grains. These dark domains are often corroded and always overgrown by light-CL oscillatorily zoned zircon forming the main zircon record.

Some of the dark-CL domains contain densely packed inclusions of melt, µm-sized rounded U-rich thorite [(Th, U)SiO_4], rounded and irregularly shaped yttrialite at < 2–3 µm [(Y, Th)$_2Si_2O_7$], up to 10 µm-long needles of Y-britholite [(Y, Ca)$_5$(SiO_4, PO_4)$_3$(OH, F)] and minor amounts of other minerals such as uraninite (UO_2) and a Nb-Y-U-rich pyrochlore, as well as holes in the spongy texture (Fig. 1b, e, h, i). None of these minerals have yet been found as individual accessory minerals in heavy mineral separates of Yellowstone rhyolites, previous works only describe the occurrence of zircon, apatite, chevkinite and allanite (Christiansen 2001; Hildreth et al. 1984; Vazquez et al. 2014). The mineral inclusions may follow primary growth zoning visible by BSE imaging in the dark-CL cores (Fig. 1e) or can be distributed throughout the dark-CL domain (Fig. 1b, h). Whether the holes result from opened fluid inclusions or from mineral or melt inclusions removed during polishing is unclear, as no unequivocal fluid inclusions with bubbles were observed during investigation with an optical microscope (Fig. 1c, f).

U-Pb ages

High-spatial resolution SIMS U-Pb dating reveals that zircon rim ages are within error of the Ar/Ar-eruption age for these units (Stelten et al. 2017; Troch et al. 2017). We note that we did not analyse "true" rims, because all analyses were obtained on polished cross-sectioned grains (cf. Chamberlain et al. 2013) and therefore the ages we report for rim analyses are maximum estimates for the respective eruption ages. Only one xenocrystic grain was identified, with a resorbed core that has a slightly discordant age of 2854 ± 37 Ma (^{204}Pb-corrected ^{207}Pb/^{206}Pb age). The high U contents of the dark-CL zones provide sufficient precision to resolve them from the Ar/Ar-eruption ages, whereas normal-CL cores span both the age range of dark-CL cores and Ar/Ar-eruption ages.

Trace element compositions

Trace elements in IPMJ zircons (suppl. Table 1) show typical rhyolitic signatures with elevated HREE and large Eu-anomalies and span almost the entire compositional range reported for other Yellowstone zircons (Matthews et al. 2013; Rivera et al. 2014, 2016; Stelten et al. 2015; Wotzlaw et al. 2015), albeit not extending to the most primitive compositions described by these authors. Zircons with dark-CL zones resemble those of compositional domain CD-4 described by Rivera et al. (2016), and show overall enriched trace element contents with U reaching extreme values of up to 2 wt% U. We note that these analysis points were set to avoid inclusions of U-Th- or REE-bearing minerals. REE generally correlate with U, Th, Y and P, and REE patterns are sub-parallel consistent with an invariant major and accessory mineral assemblage during magma evolution.

Three different compositional groups were distinguished by comparison with zircon compositions in equilibrium with the host melt (glasses from Silver Lake dome and Osbourne Butte, Troch et al. 2017) calculated with partition coefficients at 850–900 °C from Rubatto and Hermann (2007): CG-1 zircons (U < 283 ppm, Eu/Eu* > 0.077, Lu < 66 ppm) are less evolved, CG-2 zircons are in equilibrium (U 283–425 ppm, Eu/Eu* 0.038–0.077, Lu 66–96 ppm) and CG-3 are more evolved (U > 425 ppm U, Eu/Eu* < 0.038, Lu > 96 ppm). Additionally, we define CG-4 zircons as those zircons with dark cores that are extremely evolved (U > 1000 ppm, Eu/Eu* < 0.019, Lu > 300 ppm). Compositional groups are attributed based on which group's criteria are most often met.

High-resolution profiles by electron microprobe through selected zircon grains suggest that dark-CL domains (CG-4) are heterogeneously enriched in all analysed trace elements (P, Hf, U, Dy, Th, Er and Y). In zircons recording compositions prior to CG-4 (i.e., dark-CL zone is not the innermost

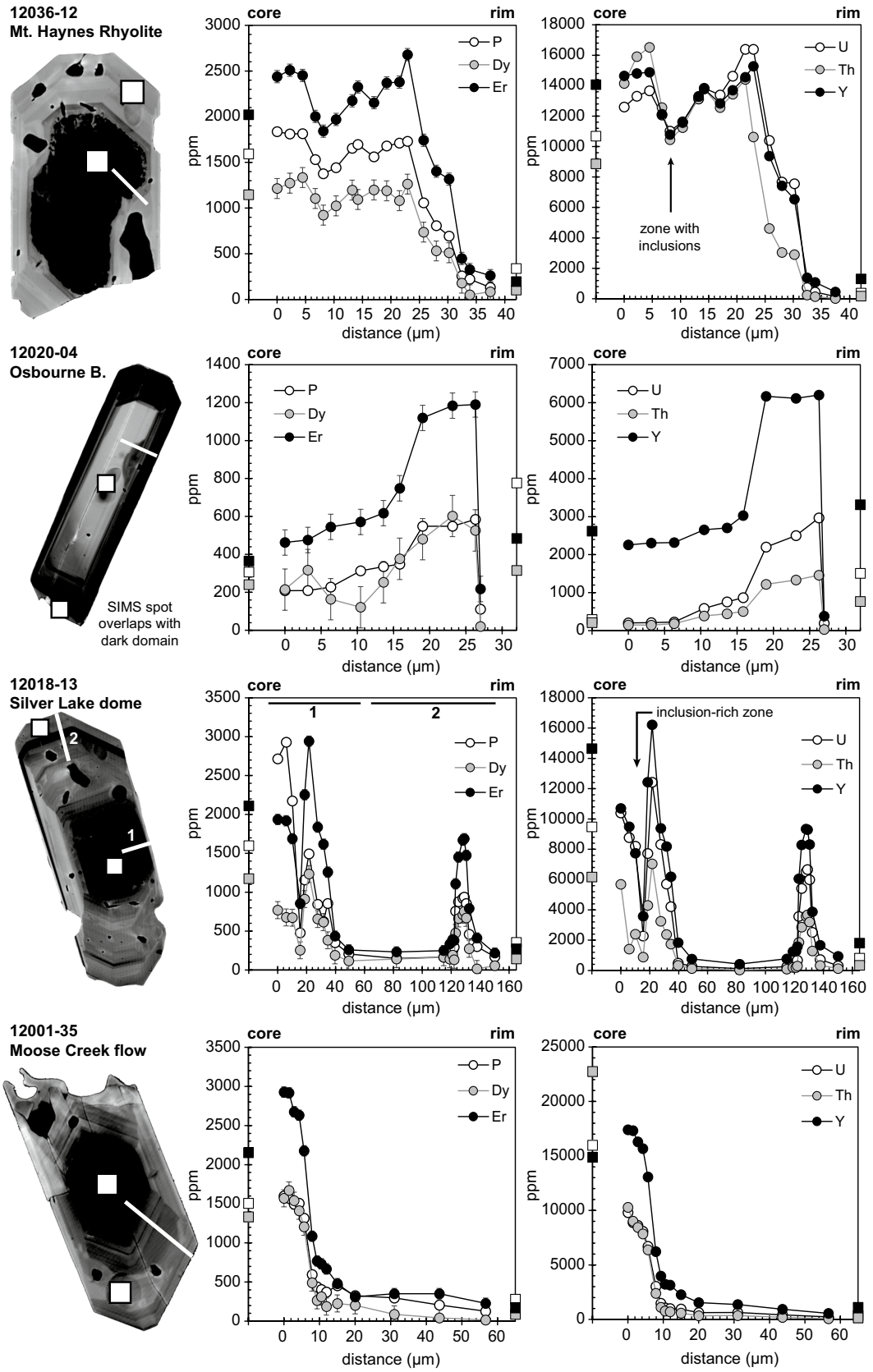
12036-12
Mt. Haynes Rhyolite
core
rim
P
Dy
Er
U
Th
Y
ppm
distance (μm)
zone with inclusions
12020-04
Osbourne B.
SIMS spot overlaps with dark domain
12018-13
Silver Lake dome
1
2
inclusion-rich zone
12001-35
Moose Creek flow

◂**Fig. 2** Trace element profiles via EPMA for selected zircons with dark-CL zones; white bars mark profile locations on grains. Boxes mark SIMS results for comparison. Note that SIMS results for rims are not true rim compositions due to their large diameter. Symbols are larger than uncertainty unless indicated by error bars. More examples can be found in suppl. Table 4. Note that ranges of both axes change between panels. Horizontal distances were calculated from coordinates of the analysis points, the uncertainty is estimated to be the reproducibility of the stage (ca. 1 µm)

core), a relatively steady increase in trace element contents towards CG-4 compositions can be observed (Fig. 2). Abrupt changes in trace elements occur where dark-CL zones are overgrown by trace element-poorer rims in equilibrium with the host melt (CG-2). Inclusion-rich dark-CL domains are depleted in trace elements compared to dark-CL inclusion-free zircon regions (Fig. 2). Trace element-rich CG-4 zircons also contain small amounts of elements such as Mg and Al, which are usually below detection limit.

Oxygen isotopes

Oxygen isotopic compositions of zircons are highly variable within each unit, with values ranging from +2.6 to +6.4‰ (Fig. 3a). Zircon $\delta^{18}O$ values in the post-caldera IP domes are slightly lower (+2.8 to +5.2‰) than those in the Lewis Canyon and Mt. Haynes Rhyolite (+3.3 to +6.4‰). The transitional Moose Creek unit (+2.6 to +4.4‰) again reveals a strong affinity with the lower-$\delta^{18}O$ domes, as was found before in other mineral groups (Troch et al. 2017). Zircon $\delta^{18}O$ values by SIMS mimic the general evolution of increasing magma $\delta^{18}O$ values with younger eruption ages (Fig. 3a), tracing the recovery towards normal-$\delta^{18}O$ magmatic values (+5.8 to +6.3‰) after initial lowering in $\delta^{18}O$ caused by caldera collapse and subsequent assimilation of hydrothermally altered roof material (Bindeman and Valley 2001; Hildreth et al. 1984; Troch et al. 2017). In all units, rims are homogenous within analytical uncertainty (±0.3‰), whereas cores are more variable (±0.6‰) and can be both higher and lower than rims. Dark-CL domains are not different in oxygen isotopic composition compared to normal-CL cores (Fig. 3a), consistent with $\delta^{18}O$ profiles from other Yellowstone units (Bindeman et al. 2008). Generally, caldera-related explosive units HRT, MFT and LCT erupting normal-$\delta^{18}O$ melt seemingly contain fewer zircons with high U contents (> 1000 ppm) than variably ^{18}O-depleted effusive inter-caldera lavas and domes, including the IPMJ record (Fig. 3b).

Raman spectra

Raman spectra of CG-1 to CG-3 zircons show the theoretically predicted peaks for zircon at 1007 cm^{-1} (Si-O v_3 stretching), 975 cm^{-1} (Si-O v_1 stretching), 438 cm^{-1} (Si-O v_2 bending), 393 cm^{-1} (external mode) and three smaller peaks at 225, 214 and 202 cm^{-1} (Fig. 4a). In these crystals, peaks are well-defined with full-width half maximum (FWHM) values of 5.6–7.0 for the 1007 cm^{-1} peak. With increasing trace element contents, these peaks decrease in intensity and become wider (FWHM 6.5–12.6 for CG-4 zircons with > 1000 ppm U, Fig. 4b). Additionally, numerous new peaks develop between 450 and 970 cm^{-1}, which can be attributed to photoluminescence associated with increased contents of REE (Lenz et al. 2015). In dark-CL zircon domains with U-Th-REE-mineral inclusions, these photoluminescence signals appear less developed and regular zircon Raman bands are narrower compared with dark-CL zircon domains without inclusions, correlating with the trend towards lower trace element contents of zircon in inclusion-rich zones.

Discussion

Zircon compositional evolution

Trace element model

The trace elements in IPMJ zircons show a continuous compositional spectrum, and we use the previously defined compositional groups (from CG-1 to CG-4) solely for the purpose of referring to different stages along this compositional evolution. Geochemical models can be used to illustrate the differentiation-driven evolution of trace element compositions in zircon, which is controlled by the trace element composition of the melt that these crystals grow from, as well as the partitioning behaviour of these elements during crystallisation. Partition coefficients for trace elements in zircon are affected by a number of processes such as temperature changes (Rubatto and Hermann 2007), availability of elements for stoichiometric mass-balance (Hoskin et al. 2000), the chemical composition of the magma and possible non-Henrian behaviour of trace elements in zircon (dependence on trace element concentration). A full discussion of the effect of these parameters is beyond the scope of this paper; here, we consider only the simple case of temperature- and concentration-independent partition coefficients, which are internally derived from the units in this study. We note that high-concentration elements (e.g., U, Th) generally vary linearly with lower-concentration elements (cf. Watson 1985), suggesting that partitioning follows Henrian behaviour even for the most evolved compositions.

Partition coefficients for Yellowstone-type magmas are established from those units where co-erupted melt could be analysed (OB, SL) by comparing glass compositions with those of the outermost zircon rims (suppl. Table 5) and exclude outliers by applying a statistical outlier test (Grubbs 1969). An average partition coefficient is then used

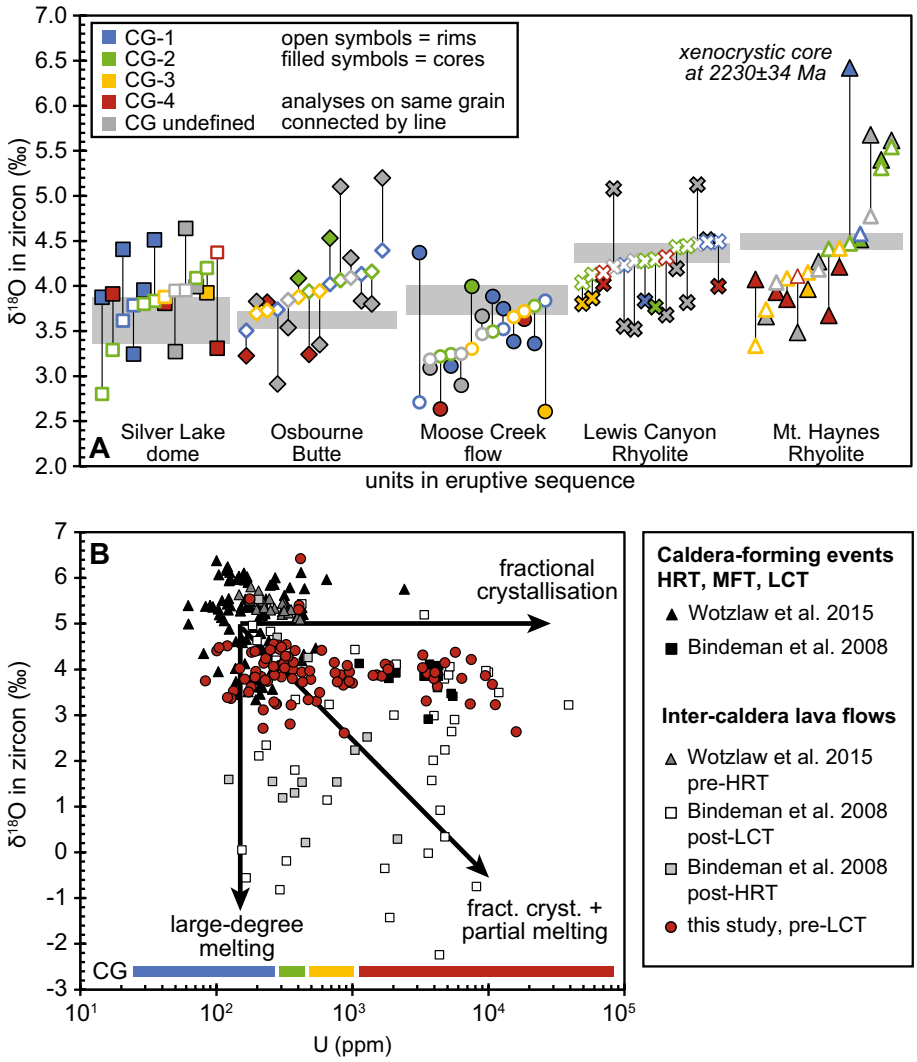

Fig. 3 **a** $\delta^{18}O$ values in zircon with units roughly arranged in stratigraphic order. Points are colour-coded for their trace element composition as defined in the trace element results section; shapes refer to different units. Grey bars mark equilibrium range with melt as identified from quartz and sanidine laser fluorination analyses (Troch et al. 2017). **b** $\delta^{18}O$ values in zircon relative to their U content as analysed by SIMS with typical uncertainty of 0.2–0.4‰. Arrows indicate possible evolutionary trends dominated by fractional crystallisation or different degrees of partial melting and assimilation of hydrothermally altered low-$\delta^{18}O$ rhyolite with relatively low U contents similar to those recorded in voluminous caldera-forming deposits in Yellowstone

throughout the fractional crystallisation model. Two different starting compositions are considered: (1) the most primitive zircons in Yellowstone from Rivera et al. (2014) (Model 1a) and Wotzlaw et al. (2015) (Model 1b), and (2) zircon in equilibrium with the co-erupted melts (CG-2) in SL (Model 2a) and OB (Model 2b). For both starting compositions, we use a near-eutectic phase assemblage (31% K-feldspar, 39% quartz, 30% plagioclase) and consider two scenarios of accessory mineral crystallisation, either zircon only (0.02%) or zircon (0.02%) plus allanite/chevkinite (0.01%), which are common accessories in Yellowstone magmas (Christiansen 2001). Mafic minerals such as pyroxene and Fe-Ti oxides only occur as minor phases in these lavas (Troch et al. 2017) and are therefore not considered. All parameters and calculation steps can be found in suppl. Table 5. Based on Zr contents in glass compositions of the erupted rhyolites, we estimate a maximum amount of 0.029% zircon can be present in the crystallising assemblage without exhausting Zr before the end of crystallisation.

The results suggest that compared to the most primitive compositions recorded in Yellowstone zircons, IPMJ magmas have already experienced 60–80% fractionation by the time they erupt (CG-2). This is consistent with large negative Eu-anomalies in the erupted melt compositions indicating extensive plagioclase fractionation. The model results also show that reaching the highest trace element contents (CG-4) is difficult within a single fractionation step for many elements (e.g., Th, Fig. 5). The melt co-erupted with IPMJ zircons would require additional 80% fractional crystallisation to reach CG-4 compositions and > 95% to reach the most U-rich values. These results are consistent with estimates from other workers, such as the range of 80–95% from Rivera et al. (2016) and > 98% from Bindeman et al. (2008). Due to the uncertainties in starting composition, fractionating assemblage and partition coefficients, we caution against linking these compositions directly to different degrees of crystallisation. Regardless of the exact pathway, these calculations illustrate clearly that the zircons sample a variety

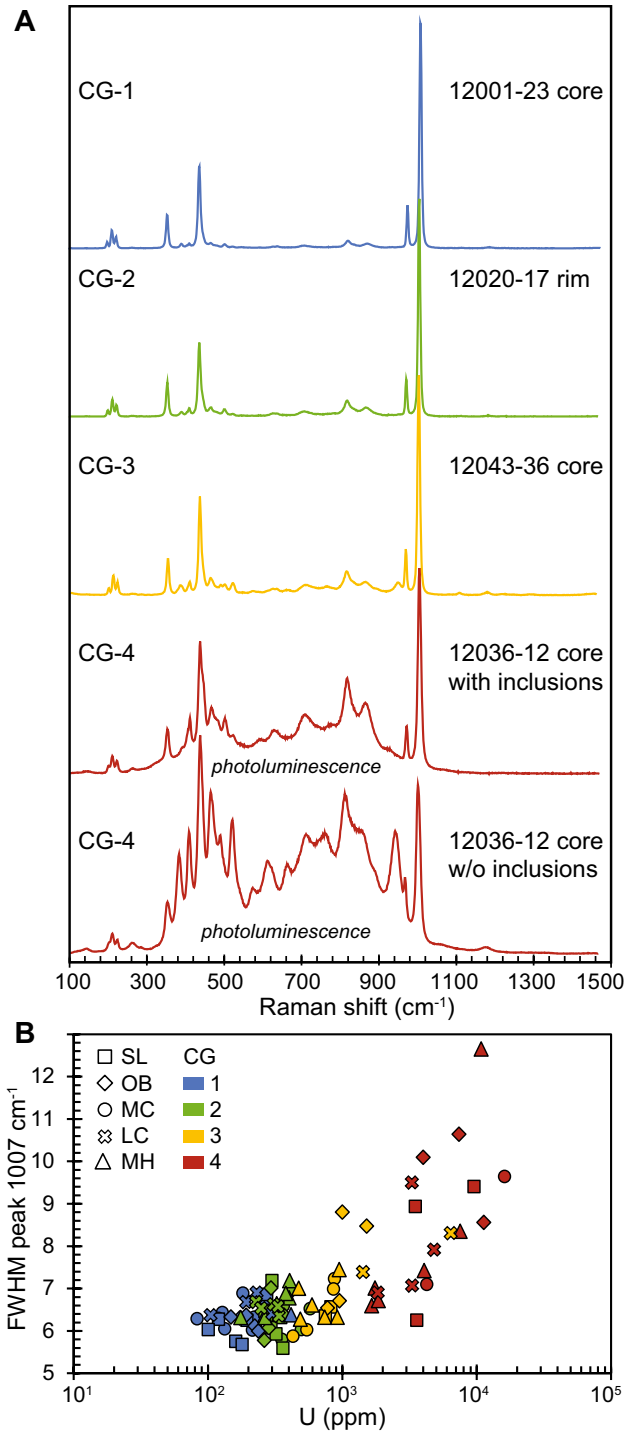

Fig. 4 **a** Raman spectra for zircon domains of different compositional groups (CG 1–4). Note the difference between CG-4 domains with inclusions and those without. **b** Full-width half maximum values for main zircon peak at 1007 cm^{-1} against U contents indicates that peaks become wider in zircon domains with higher trace element contents

of magmatic environments and record melt compositions that can be both less and more evolved than the host melt. The models also suggest that CG-4 zircons crystallised in extremely fractionated environments.

Ti-in-zircon crystallisation temperatures

A down-temperature differentiation trend for IPMJ zircons is also supported by the relative changes in Ti-in-zircon temperatures (Ferry and Watson 2007), although we advise against using absolute numbers due to poor constraints on the Ti activity in the Yellowstone units. Ti solubility models (Hayden and Watson 2007) applied on bulk rock compositions suggest an average Ti activity of 0.59, which is consistent with previous Yellowstone studies, such as the 0.55 suggested based on similarity with other silicic systems (Rivera et al. 2014, 2016; Wotzlaw et al. 2015) and the 0.56 as the highest a_{TiO2} calculated from Fe–Ti oxides (Vazquez et al. 2009). With these estimates, Ti-in-zircon temperatures would be 779 ± 36 °C (average ± standard deviation) for CG-1 zircon domains, 744 ± 30 °C for CG-2, 715 ± 34 °C for CG-3 and 748 ± 53 °C for CG-4. However, when using glass compositions as input for Ti solubility models, an average Ti activity of 0.31 is estimated for SL and OB, similar to the lowest a_{TiO2} of 0.33 by Vazquez et al. (2009) and the 0.3 estimated from Ti solubility models by Matthews et al. (2015). Ti-in-zircon temperatures would be 848 ± 40 °C for CG-1 zircon domains, 808 ± 35 °C for CG-2, 776 ± 39 °C for CG-3 and 813 ± 60 °C for CG-4. In this case, the temperature estimate for CG-2 zircon domains in equilibrium with the co-erupted melt agrees well with independently constrained pre-eruptive temperature estimates for these units (780–800 °C, Troch et al. 2017).

Temperature estimates for CG-4 zircon domains scatter strongly and Ti concentrations show a sudden change in slope at U > 1000 ppm (Fig. 6), whereas other trace elements are consistently and continuously enriched with increasing U and Th. The offset in apparent Ti-in-zircon temperatures has been previously noted by Matthews et al. (2015) who attributed it to crystal chemical effects associated with sector zoning or high U concentrations (Reid et al. 2011). The clear change in correlation between Ti and U contents in the IPMJ zircons implies a change in partitioning behaviour for Ti once a certain trace element content is reached. The consequences of trace element substitutions on the lattice structure are discussed in more detail in the following paragraphs. As (1) CG-4 composition is the logical continuation of the consistent trend from CG-1 to CG-3 for all other elements and (2) this trend is most simply explained by an evolution via fractional crystallisation (see previous section), we interpret CG-4 zircon domains as recorders of extremely fractionated lower-temperature crystallisation environments. In these unusual melt environments, commonly applied

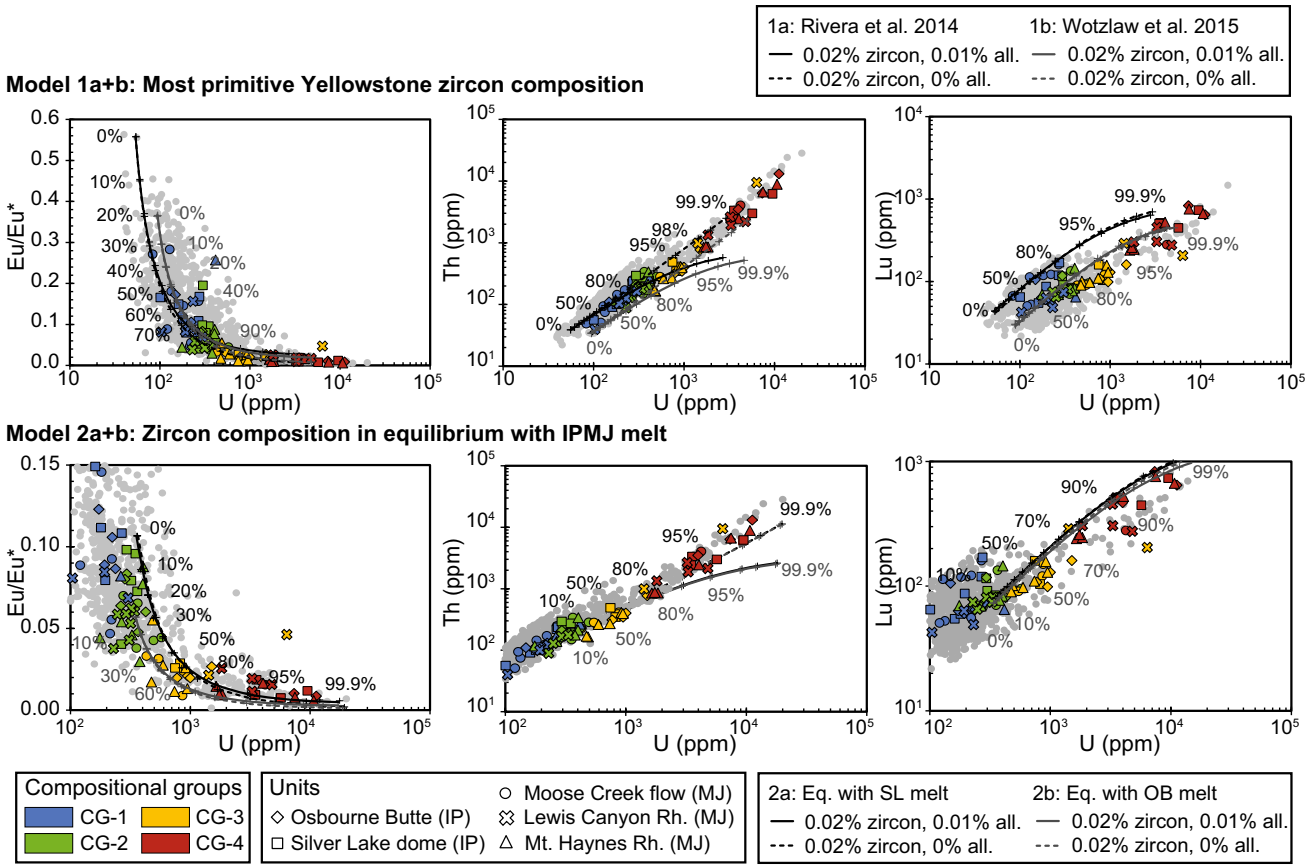

Fig. 5 Trace element model for evolution of zircon composition during fractional crystallisation of a eutectic phase assemblage (31% K-feldspar, 39% quartz, 30% plagioclase) and accessory zircon ± allanite. Starting composition for Model 1a + b is the most primitive zircon composition measured in Yellowstone zircons, starting composition for Model 2a + b is the calculated composition of zircon in equilibrium with melt as recorded by glass compositions in Silver Lake dome (SL) and Osbourne Butte (OB). Suppl. Table 5 lists the partition coefficients of all phases used in this model. Grey points in the background are reference data for zircons from other Yellowstone units (Wotzlaw et al. 2015; Stelten et al. 2015; Rivera et al. 2014, 2016; Matthews et al. 2015)

thermometers do not adequately reflect the partitioning behaviour of Ti in zircon and therefore may provide misleading results with overestimated temperatures.

Origin of dark-CL high-U zircon domains

Radiation dosage and lattice strain

Compared to normal-CL zircons, Raman spectra of the dark-CL domains show both wider regular peaks and the occurrence of additional modes (Fig. 4). Two different processes can be invoked to explain the observed difference in peak shape: (1) metamictisation due to radioactive decay, and (2) increased lattice strain due to high contents of non-stoichiometric trace elements.

Widened peaks in Raman spectra are commonly observed with beginning metamictisation of zircon (Anderson et al. 2008; Zhang et al. 2000); this widening is often illustrated by increasing FWHM values of the 1007 cm^{-1} peak. While usually limited to relatively old zircons which accumulated radiation damage over long timespans, metamictisation could also occur in young crystals with such exceptionally high U- and Th-contents as observed in the CG-4 zircons. The radiation dosage that dark-CL U- and Th-rich areas were exposed to can be calculated from their age and respective U- and Th-contents following the equation from Holland and Gottfried (1955) and Murakami et al. (1991), which results in values ranging from 0.004 to 0.118×10^{15} α-events/mg. This is much lower than the cumulative ~ 10^{16} α-events/mg required to render zircon metamict (Holland and Gottfried 1955; Murakami et al. 1991; Weber et al. 1994).

Alternatively, the observed weakened stretching mode of Si–O could be due to the high trace element contents in these dark-CL cores, leading to a distortion of the crystal lattice that results in wider Raman peaks. This is consistent with observations that incorporation of high amounts of non-stoichiometric trace elements such as Hf, Th, U, Ti, Nb, Ta, P, Y and REE is accompanied by an increase

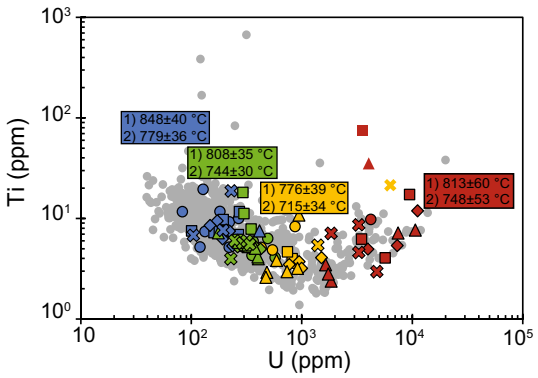

Fig. 6 Ti and U contents in IPMJ zircons (coloured) and reference data (Wotzlaw et al. 2015; Stelten et al. 2015; Rivera et al. 2014, 2016; Matthews et al. 2015). Boxes indicate average value and standard deviation for Ti-in-zircon temperatures (temperature estimate 1 with $a_{TiO2}=0.31$; estimate 2 with $a_{TiO2}=0.59$) in each compositional group; analysis points without black rim are not considered in this average. Please refer to text for a discussion of these temperatures. Possibly due to changes in partitioning behaviour of Ti, a change in slope occurs for CG-4 zircons, resulting in misleadingly high temperature estimates (red box)

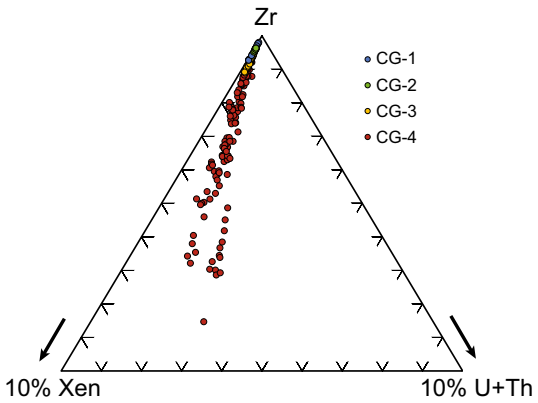

Fig. 7 Ternary diagram showing variable degrees of xenotime (Y + P + REE) and coffinite-thorite (U + Th) substitution in IPMJ zircons based on molar contents of trace elements in zircons analysed by EPMA. REE in microprobe data consist of Dy and Er, which commonly make up 1/3 of all REE in Yellowstone zircons

in lattice parameter dimensions (Zeng et al. 2017). Quadrivalent U, Th and Hf can be exchanged directly with Zr^{4+} without requiring additional elements for charge balance, for example, by coupled coffinite–thorite substitution with $U^{4+} + Th^{4+} \leftrightarrow 2\,Zr^{4+}$. The most common substitution mechanism to incorporate REE in zircon is the xenotime-substitution, with $(Y, REE)^{3+} + P^{5+} \leftrightarrow Zr^{4+} + Si^{4+}$ (Hanchar et al. 2001; Hoskin et al. 2000; Speer 1980). Molar abundances of U, Th, Y and P in the IPMJ dark-CL domains are sufficiently high to consider these cores as zircon solid solutions with both xenotime and coffinite-thorite endmembers (Fig. 7); CG-4 zircons contain up to 5% xenotime component and 2% coffinite-thorite component. However, ratios of (Y + REE)/P ratios are > 1 for all zircons, indicating that pentavalent P^{5+} alone cannot charge balance the increased concentrations of REE and Spandler et al. (2004) propose that interstitial substitution of monovalent Cl^-, F^- and OH^- together with complex coupled substitutions (e.g., Mg, Al, Fe) control the uptake of REE into zircons. The additional strain imposed on the crystal lattice by each of these substitution mechanisms is generally assumed to also affect the partitioning of trace elements on other sites, and the uptake of trace elements will be ultimately limited by the strain that the crystal lattice can accommodate (e.g., Blundy and Wood 1994). With the IPMJ zircons being too young to have experience significant cumulative radiation damage and the widening of Raman peaks strongly correlating with trace element contents, we conclude that increased lattice strain due to incorporation of high amounts of trace element contents is responsible for the increased FWHM values of Raman peaks in CG-4 zircons.

An example for the dependence of the partitioning behaviour of a single element on the crystal lattice strain is the observed change in Ti partitioning (Fig. 6). Ti is generally incorporated in the fourfold coordinated Si^{4+} site in zircon but has a slightly larger ionic radius (0.42 Å) than Si^{4+} (0.26 Å, Shannon 1976). The observed stretching in Si-O bonds as indicated by Raman spectra (Fig. 4) could facilitate substitution of the larger Ti^{4+} ion in CG-4 zircon domains compared to the partitioning behaviour in regular magmatic zircons with lower trace element contents. Similarly, the partitioning of Hf in zircon changes from a clear correlation between Hf and U for CG-1 to CG-3 towards more chaotic behaviour for CG-4 zircons.

REE-mineral inclusions

Previously undescribed, we find for the first time that some of the dark-CL zones in Yellowstone zircons contain REE- and U-Th-rich mineral inclusions (yttrialite, britholite, thorite–coffinite, and others). Around the inclusions, the backscatter and CL patterns often look disturbed or show schlieren, and Raman spectra show more well-defined peaks for inclusion-bearing dark-CL domains compared to inclusion-free dark-CL zones (Fig. 4). In some grains, the inclusions follow primary growth zones ("ghost textures"), whereas neighbouring zones with lower trace element contents remain inclusion-free. Two possible scenarios could explain the presence of inclusions, either (1) capturing of accessory phases during crystal growth, or (2) dissolution-reprecipitation in the presence of a fluid or melt phase.

The onset of crystallisation of accessory U-Th-rich phases which are subsequently captured in the zircon during crystal growth could explain several of the observed features in IPMJ zircons, particularly the concentration of inclusions along growth zones that also contain melt inclusions (e.g.,

Fig. 1e). Co-crystallisation of coffinite, thorite and yttrialite would result in removal of trace elements from the melt and lead to crystallisation of slightly trace element-poorer zircon regions. Lattice strain would consequently be reduced, as the need to incorporate high amounts of trace elements is eliminated. However, it seems difficult to envisage what kind of mechanism could lead to the sudden beginning and ceasing of accessory mineral saturation that the textures would imply in such case, which is inconsistent with the lack of these minerals as independent phases or as inclusions in other minerals.

With many of the inclusion phases being isostructural with zircon, the inclusion textures resemble dissolution-reprecipitation patterns described by Geisler et al. (2007). Dissolution followed by reprecipitation would suggest that the original U- and Th-contents may have been as high as the sum of U- and Th-contents in zircon and its inclusions, but zircon subsequently recrystallized into a trace element-poorer zircon phase and U-Th-bearing silicate inclusions. Coupled dissolution-reprecipitation thus transforms metastable U-Th-rich zircon with wide Raman peaks into stable U-Th-poorer zircon with reduced lattice strain (narrower Raman peaks). In this case, the distribution of inclusions along primary growth zones suggests that dissolution-reprecipitation is limited to metastable highly enriched zircon regions where trace element contents exceed the threshold of trace element contents that can be accommodated in the zircon crystal structure long-term under the prevailing conditions. Geisler et al. (2007) suggest that due to the extremely slow diffusive exchange in zircon, recrystallisation is limited to equilibrative exchange in the presence of a fluid phase, which may also be responsible for corrosive rims around some of the dark-CL domains. They note that re-equilibration of zircon may equally happen in the presence of a melt phase; however, no unambiguous demonstration of a reaction with a melt phase exists to this day (Geisler et al. 2007). We note that all dark-CL zircon domains are overgrown by light-CL rims that are in equilibrium with the eruptive melt, thus there is clear evidence that these cores have been in contact with a melt phase. Additionally, many of the inclusion-rich cores also contain melt inclusions. While we do not find unequivocal evidence for fluid inclusions in these grains, the porous and spongy textures show the potential for interaction with a fluid phase. The recycling of dark-CL zircons into the eruptive host melt may be responsible for the decrepitation of fluid inclusions if these were originally present in the dark-CL zircon domains.

Independent of the mechanism that creates the observed inclusions, they require an environment that successfully stabilises these U-Th-silicate phases. Additional insights into the growth environment of the dark-CL highly enriched zircons can therefore be gained by comparing these grains with similar crystals from other settings.

Implications for growth environment

Common low-temperature near-solidus origin for dark-CL zircon domains

While dark-CL zircon domains with elevated uranium contents have been reported from highly evolved volcanics [e.g., Devils Kitchen Rhyolite in California (Miller and Wooden 2004), the Sierra Madre Occidental Province in Mexico (Bryan et al. 2008) and the Taupo Volcanic Field in New Zealand (Charlier et al. 2005)], they are much more commonly reported from plutonic and/or ore-related granitic systems. Furthermore, the REE- and U-Th-rich inclusions inside the dark-CL zircon zones are only visible in backscatter imaging, not in CL mode, and therefore it is conceivable that they are commonly overlooked during standard zircon preparation techniques that only involve CL imaging. We therefore doubt that the presence of these inclusions is limited to the IPMJ lavas of Yellowstone or Yellowstone in general, and they may be similarly abundant in other highly evolved silicic settings.

Dark-CL zones associated with high contents of non-stoichiometric elements in zircon are described in a variety of plutonic rocks, such as a granitic suite associated with Li-F-granites (ongonites) in the Russian Far East where zircons commonly exhibit dark-CL rims and inclusions of uraninite, thorite, yttrialite and other phases (Alekseev et al. 2014), metagranites from the Western Tauern Window and Ötztal-Stubai Crystalline complex in the Eastern Alps where overgrowth dark-CL rims with nanopores are observed in zircons (Kovaleva et al. 2017), dark-CL U-Th-rich zircon domains in the late-stage Guyangzhai granite intrusion in South China (Wang et al. 2017) and dark-CL inclusion-rich zircons with widened Raman peaks in A-type granites from Xiangshan, North China (Zeng et al. 2017). Zircon solid solutions with thorite–xenotime–coffinite endmembers have also been described in Variscan leucogranites of the German Erzgebirge and Pan-African granites from Jordan (Förster 2006).

The common occurrence of dark-CL zircon domains in granitic systems supports an origin in a highly fractionated environment, as indicated by our first-order trace element fractionation model (Section "Trace element model", Fig. 5). In such an environment, elements like U, Th and REE are sufficiently enriched to be forced into the zircon structure. Although zircon solid solutions generally require higher temperatures for equilibrium formation than their endmembers due to the required excess mixing enthalpy (Ferriss et al. 2010), incorporation of non-stoichiometric trace elements into zircon seems to be enhanced in highly evolved lower-temperature melts. In particular, the fact that dark-CL zircon domains often occur as rims in plutonic rocks, whereas they are overgrown by normal-CL rims in

Yellowstone zircons, supports our conclusion that these zircons originate from highly fractionated near-solidus pockets (80–95% crystallised, see "Trace element model"). In plutonic rocks, the zircon rims record the end stage of magmatic differentiation, whereas in the volcanic record the grains are remobilised and entrained into the melt that they erupted with. In this sense, these highly enriched zircons make a strong case for a close genetic relationship between plutonic and volcanic rocks of granitoid compositions and support the origin of Yellowstone rhyolite lavas as being derived from melt batches within a long-lived highly crystalline mushy host system, as supported by geochronological and petrological studies (Stelten et al. 2015; Troch et al. 2017; Vazquez et al. 2009; Wotzlaw et al. 2015), as well as geophysical imaging of the melt body currently underlying Yellowstone (e.g., Husen et al. 2004). A broad evolution whereby the enrichment in trace elements is dominantly driven by fractional crystallisation is not in contrast to previous descriptions of the majority of Yellowstone zircons being reversely zoned (Matthews et al. 2015). Rather than resulting from progressive melting, the reverse zoning in many of the Yellowstone zircons may be due to the overgrowth rims being in equilibrium with the host melt (CG-2), which we have shown to be less evolved than that recorded in many zircon cores (CG-3 and 4).

Magmatic–hydrothermal transition

In many cases that describe dark-CL zircon domains with high contents of REE and High Field Strength Elements (HFSE), these have been associated with a volatile-rich origin, such as magmatic–hydrothermal, hydrothermal or pegmatitic environments, e.g., hafnian zircon in the Li–Cs–Ta granitic pegmatite in Altai, northwestern China (Yin et al. 2013), U-Th-Y-REE-enriched hydrothermal zircons from the Boggy Plain zoned pluton (Hoskin 2005) and U-Th-rich hydrothermal granite-hosted zircons from the Weondong deposit, South Korea (Park et al. 2016). Some authors infer elevated OH and F contents in dark-CL zircons (Zeng et al. 2017). However, it is difficult to assess whether this is a true reflection of the melt or fluid that these crystals grew from or simply a consequence of charge balancing elevated REE in the zircon structure, or a combination of these processes. In the following discussion, we use the term *magmatic* for environments dominated by volatile-undersaturated melt, *magmatic–hydrothermal* where melt co-exists with aqueous fluid (e.g., volatile-saturated melt), and *hydrothermal* for environments dominated by aqueous fluid, either from exsolved magmatic volatiles or surface-derived meteoric water.

The inclusion-rich, spongy texture of dark-CL zircon domains with high contents of HFSE and REE fulfils criteria that have been used to identify zircon crystallised from aqueous fluids (Corfu 2003; Hoskin et al. 1998). However, Pettke et al. (2005) and Schaltegger (2007) note that textural and compositional parameters alone cannot unequivocally distinguish hydrothermal from magmatic zircon, so identification of hydrothermal zircon requires them to be found in typical hydrothermal mineral assemblages. Naturally, these would not preserved if zircons are subsequently entrained into a magma. As pointed out before, crystallisation of U-Th-REE-phases within the zircon crystals requires an environment in which these minerals are stable. A comparison of the settings, in which these minerals are commonly found, may therefore provide valuable insights into their preferred growth environment. In silicic systems, REE- and U-Th-bearing minerals are commonly associated with late-magmatic hydrothermal fluids or residual melts related to A-type granitoid intrusions or associated volcanics (e.g., Allaz et al. 2015; Castor and Henry 2000; Chakhmouradian and Zaitsev 2012). Van Lichtervelde et al. (2009) attribute the occurrence of Ta-mineral inclusions in REE-rich zircon to dissolution–reprecipitation in the presence of aqueous fluid at sub-solidus temperatures, whereas Ta can be accommodated in the crystal structure at common magmatic temperatures. A similar process is invoked for the occurrence of thortveitite, yttrialite and xenotime inclusions in Sc-REE-rich zircons (Spandler et al. 2004). It, therefore, is conceivable that dark-CL REE-rich zircon domains originate in late-stage volatile-rich residual melts, and that dissolution–reprecipitation that forms trace element-poorer zircon and mineral inclusions proceeds at slightly lower temperatures in the presence of a fluid phase.

Tracing the melt-fluid interaction by zircon trace element compositions is difficult, because at low pressures (~ 1 kbar), the system water-melt is thought to be characterised by a solvus at a temperature of 710 °C (Thomas et al. 2000). At near-solidus temperatures (500–700 °C), water-rich silicic melts and silica-rich hydrothermal fluids therefore resemble each other sufficiently to show very similar partitioning behaviour (Pettke et al. 2005). Additionally, the fluid phase will split into a two-phase fluid consisting of vapour and brine between 400 and 1100 bar and 650–800 °C depending on the NaCl content (Driesner and Heinrich 2007; Veksler et al. 2002), which complicates the application of published single-phase fluid/melt partitioning coefficients on trace element models (London et al. 1988; Webster et al. 1989; Zajacz et al. 2008). Exsolution of a magmatic fluid phase can also not be identified by changes in zircon $\delta^{18}O$ values, because $\Delta^{18}O$ fluid-melt approaches zero at temperatures > 450–500 °C (Bindeman 2008). The lack of lower $\delta^{18}O$ values in dark-core CG-4 zircons thus only precludes them from being derived from hydrothermal meteoric fluids with very low $\delta^{18}O$-values [meteoric water in Yellowstone estimated at − 19‰ (Hildreth et al. 1984)]. However, published melt-fluid partition coefficients suggest that REE as well as U

and Th preferentially partition into the melt phase, whereas elements such as P, Cl, F and Li that commonly substitute into zircon to charge balance REE, show an affinity for the fluid phase (London et al. 1988; Webster et al. 1989; Zajacz et al. 2008). Exsolution of large amounts of P-Cl-F-bearing fluid at temperatures < 710 °C would, therefore, reduce the ability of zircon to accommodate non-stoichiometric trace elements, if it crystallises from residual melt; this could drive the crystallisation of U-Th-REE-mineral phases during dissolution–reprecipitation reactions. A removal of P is, for example, indicated by the finding that none of the inclusions contain phosphate minerals, although inclusion-free (i.e., pre-recrystallisation stage) CG-4 zircons show very high P contents (up to 1.6 wt% P).

Pre-eruptive storage conditions for IPMJ rhyolites have previously been identified as close to water saturation at 1 kbar, 770–800 °C and ~ 60–80% melt fraction at initial 3 wt% H_2O (Fig. 8b, Troch et al. 2017). We have shown that enriched trace element contents in CG-4 zircon domains require significantly more evolved storage conditions (> 90% crystallisation, this

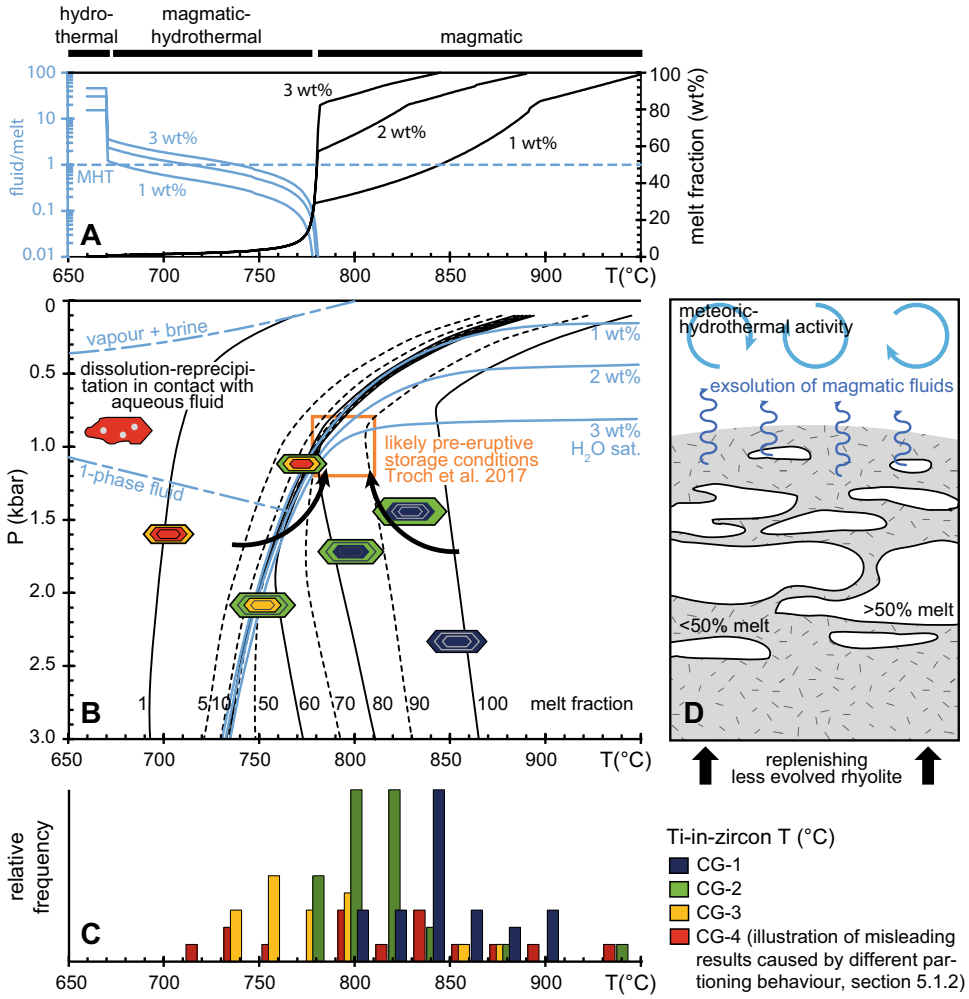

Fig. 8 **a** Fluid-melt ratios by mass (blue lines) for different initial H_2O contents (1, 2, and 3 wt%) based on rhyolite-MELTS simulations starting with Osbourne Butte bulk composition at 1 kbar, QFM-buffered. Black lines indicate melt fractions (right *y*-axis) for the same runs. These simulations identify the three regimes hydrothermal (no melt), magmatic–hydrothermal (fluid-saturated) and magmatic (fluid-undersaturated). Blue dashed line shows magmatic–hydrothermal transition (MHT, fluid/melt changes from < 1 to > 1). **b** Exemplary origins of zircons with different compositional domains (CG-1 to -4) from different magmatic regimes as modelled by rhyolite-MELTS (position of zircons along y-axis is arbitrary). Black lines indicate melt fractions at 3 wt% initial H_2O content, blue lines show H_2O saturation for different initial water contents. Blue dashed lines indicate P-T-range in which 1-phase fluid will separate into vapour and brine depending on NaCl content (calculated with SoWat software, Driesner and Heinrich 2007). Orange box indicates likely pre-eruptive storage conditions for IPMJ rhyolites as identified in Troch et al. (2017). **c** Frequency distribution diagram for Ti-in-zircon temperatures (Ferry and Watson 2007) calculated with $a_{TiO2} = 0.31$ for different compositional groups. Note that temperature estimates for CG-4 are only shown to illustrate the effect of different Ti partitioning behaviour on Ti-in-zircon temperatures; crystallisation temperatures for CG-4 zircons are likely lower than those for CG-3 zircons. **d** Illustration of magmatic, magmatic–hydrothermal and hydrothermal regimes in a mushy magmatic reservoir

study; 98% crystallisation, Bindeman et al. 2008; 80–95% crystallisation; Rivera et al. 2016), which therefore necessarily includes zircon growth in a water-saturated regime. Fractional crystallisation and a down-temperature magma evolution will lead to exsolution of a fluid phase as soon as the concentration of water exceeds the water saturation threshold of the remaining melt at the relevant P-T-conditions. Rhyolite-MELTS simulations using the bulk composition of Osbourne Butte (Troch et al. 2017) as a starting composition indicate that the formation of a free fluid phase occurs during a small temperature interval with high degrees of crystallisation (between 770 and 790 °C crystallisation of 23–77% for different H_2O contents, Fig. 8a, b). As the initial water content is a major control for the melt fraction at a given temperature, the fluid phase appears at variable crystallinities for different initial water contents. The temperature, below which a volatile-rich melt co-exists with minor amounts of aqueous fluid, is relatively constant. With continuing crystallisation, the system then changes from a melt-dominated into a fluid-dominated environment at temperatures between 670 and 740 °C (fluid/melt ratio > 1, Fig. 8a), marking the magmatic–hydrothermal transition.

These simulations suggest that at the crystallinities required to produce the observed trace element enrichment in CG-4 zircons, the host melt will be volatile-saturated. Accessory hornblende and biotite found in some IPMJ rhyolites may be derived from such volatile-rich melts that fractionated beyond erupted melt compositions. The uniform enrichment in trace elements in CG-4 zircons coupled with the textural information and unchanged $\delta^{18}O$ values would therefore be consistent with growth from volatile-saturated low-temperature melts (~ 680–770 °C, Fig. 8). The dominance of large amounts of exsolved fluid over small amount of remaining silicic melt at temperatures below the magmatic–hydrothermal transition may be responsible for large-scale segregation of fluid-compatible P, Cl, F, Li, which are subsequently unavailable for charge balancing substituted trace elements. Recrystallisation of zircon in such an environment may lead to the formation of U-Th-REE-rich silicate mineral inclusions, which record magma reservoir environments not commonly sampled by volcanic eruptions. The potential of highly fractionated rhyolite magmas to concentrate REE, U and Th (Jowitt et al. 2017) and the occurrence of U-Th-REE-rich mineral inclusions could make these zircons prime examples for syn-magmatic ore mineralisation, as has been observed in other settings (Buret et al. 2017).

Conclusions

Zircons from the Island Park-Mount Jackson Rhyolite series sample a variety of magmatic environments that are both more and less evolved than co-erupted melt compositions. Trace element compositions can be explained by fractional crystallisation, with the most enriched CG-4 zircon domains with > 1000 ppm U requiring extremely fractionated environments (> 95%). Substitution of high amounts of trace elements in CG-4 zircons with dark-CL cores leads to distortion of the crystal lattice that can be traced by Raman spectroscopy and may affect Ti partitioning and derived Ti-in-zircon temperatures. U-Th-REE-rich mineral inclusions within dark-CL zircon domains are likely derived from dissolution–reprecipitation processes in the presence of a fluid phase, which enhances U-Th-REE-mineralisation due to uptake of elements required to charge balance REE in zircon. The presence of dark-CL CG-4 zircons supports rhyolite generation within long-lived mushy host systems that contain highly crystalline, near-solidus regions saturated with a chemically complex magmatic volatile phase. Minerals from such regions can be periodically remobilised and entrained by volcanic eruptions, thereby linking the different magmatic realms (volcanic, plutonic, pegmatitic, and hydrothermal).

Acknowledgements This work has been supported by an ETH research grant (ETH-05 13-2 covering J.T.). The HIP facility at Heidelberg University is operated under the auspices of the DFG Scientific Instrumentation and Information Technology programme. We thank Christie Hendrix and Stacey Gunther from the Yellowstone National Park Service for their assistance with research permits (Yellowstone permit YELL-05940), Lukas Martin and Julien Allaz (ETH) for assistance with EPMA and Jörn-Frederik Wotzlaw for discussions. We are grateful to Ilya Bindeman, Matt Loewen and an anonymous reviewer for their constructive and careful reviews, and to Othmar Müntener for editorial handling. John Wolff, Mark Stelten, Paul Nex and Matthieu Galvez are thanked for providing additional comments on the manuscript.

References

Alekseev V, Polyakova E, Machevariani M, Marin YB (2014) Evolution of zircons from postorogenic intrusive series with Li–F granites, Russian Far East. Geol Ore Deposits 56(7):513–530

Allaz J, Raschke MB, Persson PM, Stern CR (2015) Age, petrochemistry, and origin of a REE-rich mineralization in the Longs Peak-St. Vrain batholith, near Jamestown, Colorado (USA). Am Mineral 100(10):2123–2140

Åmli R, Griffin W (1975) Microprobe analysis of REE minerals using empirical correction factors. Am Mineral 60:599–606

Anderson AJ, Wirth R, Thomas R (2008) The alteration of metamict zircon and its role in the remobilization of high-field-strength elements in the Georgeville granite, Nova Scotia. Can Mineral 46(1):1–18

Barboni M, Boehnke P, Schmitt AK, Harrison TM, Shane P, Bouvier A-S, Baumgartner L (2016) Warm storage for arc magmas. Proc Natl Acad Sci 113(49):13959–13964

Bindeman I (2008) Oxygen isotopes in mantle and crustal magmas as revealed by single crystal analysis. Rev Mineral Geochem 69(1):445–478

Bindeman IN, Valley JW (2001) Low-$\delta^{18}O$ Rhyolites from Yellowstone: magmatic evolution based on analyses of Zircons and individual phenocrysts. J Petrol 42(8):1491–1517

Bindeman IN, Fu B, Kita NT, Valley JW (2008) Origin and evolution of silicic magmatism at yellowstone based on ion microprobe analysis of isotopically zoned zircons. J Petrol 49(1):163–193. https://doi.org/10.1093/petrology/egm075

Black LP, Kamo SL, Allen CM, Davis DW, Aleinikoff JN, Valley JW, Mundil R, Campbell IH, Korsch RJ, Williams IS (2004) Improved 206 Pb/238 U microprobe geochronology by the monitoring of a trace-element-related matrix effect; SHRIMP, ID–TIMS, ELA–ICP–MS and oxygen isotope documentation for a series of zircon standards. Chem Geol 205(1):115–140

Blundy J, Wood B (1994) Prediction of crystal-melt partition coefficients from elastic moduli. Nature 372(6505):452–454

Bryan SE, Ferrari L, Reiners PW, Allen CM, Petrone CM, Ramos-Rosique A, Campbell IH (2008) New insights into crustal contributions to large-volume rhyolite generation in the mid-Tertiary Sierra Madre Occidental province, Mexico, revealed by U–Pb geochronology. J Petrol 49(1):47–77

Buret Y, Wotzlaw J-F, Roozen S, Guillong M, von Quadt A, Heinrich CA (2017) Zircon petrochronological evidence for a plutonic-volcanic connection in porphyry copper deposits. Geology 45(7):623–626

Castor SB, Henry CD (2000) Geology, geochemistry, and origin of volcanic rock-hosted uranium deposits in northwestern Nevada and southeastern Oregon, USA. Ore Geol Rev 16(1):1–40

Chakhmouradian AR, Zaitsev AN (2012) Rare earth mineralization in igneous rocks: sources and processes. Elements 8(5):347–353

Chamberlain K, Wilson C, Wooden JL, Charlier B, Ireland T (2013) New perspectives on the Bishop Tuff from zircon textures, ages and trace elements. J Petrol 55(2):395–426

Charlier B, Wilson C, Lowenstern J, Blake S, Van Calsteren P, Davidson J (2005) Magma generation at a large, hyperactive silicic volcano (Taupo, New Zealand) revealed by U–Th and U–Pb systematics in zircons. J Petrol 46(1):3–32

Christiansen RL (2001) The quaternary and pliocene yellowstone plateau volcanic field of Wyoming, Idaho, and Montana. USGS Professional Paper 729-G

Cooper KM, Kent AJ (2014) Rapid remobilization of magmatic crystals kept in cold storage. Nature 506(7489):480

Corfu F (2003) Atlas of zircons textures. Rev Mineral Geochem 53:469–500

Driesner T, Heinrich CA (2007) The system H 2 O–NaCl. Part I: Correlation formulae for phase relations in temperature–pressure–composition space from 0 to 1000 °C, 0–5000 bar, and 0–1 X NaCl. Geochim Cosmochim Acta 71(20):4880–4901

Ellis B, Mark D, Troch J, Bachmann O, Guillong M, Kent A, von Quadt A (2017) Split-grain 40 Ar/39 Ar dating: Integrating temporal and geochemical data from crystal cargoes. Chem Geol 457:15–23

Ferriss E, Ewing R, Becker U (2010) Simulation of thermodynamic mixing properties of actinide-containing zircon solid solutions. Am Mineral 95(2–3):229–241

Ferry J, Watson E (2007) New thermodynamic models and revised calibrations for the Ti-in-zircon and Zr-in-rutile thermometers. Contrib Mineral Petrol 154(4):429–437

Förster H-J (2006) Composition and origin of intermediate solid solutions in the system thorite–xenotime–zircon–coffinite. Lithos 88(1):35–55

Geisler T, Schaltegger U, Tomaschek F (2007) Re-equilibration of zircon in aqueous fluids and melts. Elements 3(1):43–50

Grubbs FE (1969) Procedures for detecting outlying observations in samples. Technometrics 11(1):1–21

Hanchar JM, Finch RJ, Hoskin PW, Watson EB, Cherniak DJ, Mariano AN (2001) Rare earth elements in synthetic zircon: Part 1. Synthesis, and rare earth element and phosphorus doping. Am Mineral 86(5–6):667–680

Hayden LA, Watson EB (2007) Rutile saturation in hydrous siliceous melts and its bearing on Ti-thermometry of quartz and zircon. Earth Planet Sci Lett 258(3):561–568

Hildreth W, Christiansen RL, O'Neil JR (1984) Catastrophic isotopic modification of rhyolitic magma at times of caldera subsidence, Yellowstone Plateau Volcanic Field. J Geophys Res 89(B10):8339. https://doi.org/10.1029/JB089iB10p08339

Holland HD, Gottfried D (1955) The effect of nuclear radiation on the structure of zircon. Acta Crystallogr A 8(6):291–300

Hoskin PW (2005) Trace-element composition of hydrothermal zircon and the alteration of Hadean zircon from the Jack Hills, Australia. Geochim Cosmochim Acta 69(3):637–648

Hoskin P, Kinny P, Wyborn D (1998) Chemistry of hydrothermal zircon: investigating timing and nature of water–rock interaction. Water Rock Interact 9:545–548

Hoskin PW, Kinny PD, Wyborn D, Chapell BW (2000) Identifying accessory mineral saturation during differentiation in granitoid magmas: an integrated approach. J Petrol 41(9):1365–1396

Husen S, Smith RB, Waite GP (2004) Evidence for gas and magmatic sources beneath the Yellowstone volcanic field from seismic tomographic imaging. J Volcanol Geotherm Res 131(3):397–410

Jowitt SM, Medlin CC, Cas RA (2017) The rare earth element (REE) mineralisation potential of highly fractionated rhyolites: a potential low-grade, bulk tonnage source of critical metals. Ore Geol Rev 86:548–562

Kovaleva E, Harlov D, Klötzli U (2017) Complicated secondary textures in zircon record evolution of the host granitic rocks: Studies from Western Tauern Window and Ötztal-Stubai Crystalline Complex (Eastern Alps, Western Austria). Lithos 284:381–400

Lenz C, Nasdala L, Talla D, Hauzenberger C, Seitz R, Kolitsch U (2015) Laser-induced REE3+ photoluminescence of selected accessory minerals—an "advantageous artefact" in Raman spectroscopy. Chem Geol 415:1–16

Li XH, Long WG, Li QL, Liu Y, Zheng YF, Yang YH, Chamberlain KR, Wan DF, Guo CH, Wang XC (2010) Penglai zircon megacrysts: a potential new working reference material for microbeam determination of Hf–O isotopes and U–Pb age. Geostand Geoanal Res 34(2):117–134

London D, Hervig RL, Morgan GB (1988) Melt-vapor solubilities and elemental partitioning in peraluminous granite-pegmatite systems: experimental results with Macusani glass at 200 MPa. Contrib Mineral Petrol 99(3):360–373

Lünsdorf N, Lünsdorf J (2016) Evaluating Raman spectra of carbonaceous matter by automated, iterative curve-fitting. Int J Coal Geol 160:51–62

Matthews N, Vazquez J, Calvert A (2013) Concordant ages for the Lava Creek Tuff from high-spatial-resolution U-Pb dating of zircon rim faces and single-crystal sanidine 40Ar/39Ar dating. AGU Fall Meeting Abstracts 1:06

Matthews NE, Vazquez JA, Calvert AT (2015) Age of the Lava Creek supereruption and magma chamber assembly at Yellowstone based on 40Ar/39Ar and U-Pb dating of sanidine and zircon crystals. Geochem Geophys Geosyst 16(8):2508–2528

Miller JS, Wooden JL (2004) Residence, resorption and recycling of zircons in Devils Kitchen rhyolite, Coso Volcanic field, California. J Petrol 45(11):2155–2170

Murakami T, Chakoumakos BC, Ewing RC, Lumpkin GR, Weber WJ (1991) Alpha-decay event damage in zircon. Am Mineral 76:1510–1532

Obradovich JD (1992) Geochronology of the Late Cenozoic volcanism of Yellowstone National Park and adjoining areas, Wyoming and Idaho. USGS Open-File Report 92–408, pp 45

Park C, Song Y, Chung D, Kang I-M, Khulganakhuu C, Yi K (2016) Recrystallization and hydrothermal growth of high U–Th zircon in the Weondong deposit, Korea: record of post-magmatic alteration. Lithos 260:268–285

Pearce NJ, Perkins WT, Westgate JA, Gorton MP, Jackson SE, Neal CR, Chenery SP (1997) A compilation of new and published major and trace element data for NIST SRM 610 and NIST SRM 612 glass reference materials. Geostand Geoanal Res 21(1):115–144

Pettke T, Audétat A, Schaltegger U, Heinrich CA (2005) Magmatic-to-hydrothermal crystallization in the W–Sn mineralized Mole Granite (NSW, Australia): Part II: evolving zircon and thorite trace element chemistry. Chem Geol 220(3):191–213

Reid MR, Vazquez JA, Schmitt AK (2011) Zircon-scale insights into the history of a Supervolcano, Bishop Tuff, Long Valley, California, with implications for the Ti-in-zircon geothermometer. Contrib Mineral Petrol 161(2):293–311

Rivera TA, Schmitz MD, Crowley JL, Storey M (2014) Rapid magma evolution constrained by zircon petrochronology and 40Ar/39Ar sanidine ages for the Huckleberry Ridge Tuff, Yellowstone, USA. Geology 42(8):643–646

Rivera TA, Schmitz MD, Jicha BR, Crowley JL (2016) Zircon petrochronology and 40Ar/39Ar sanidine dates for the mesa falls tuff: crystal-scale records of magmatic evolution and the short lifespan of a large yellowstone magma chamber. J Petrol 57(9):1677–1704

Robock A (2002) Volcanic eruptions and climate. Clim Change 38:305

Rubatto D, Hermann J (2007) Experimental zircon/melt and zircon/garnet trace element partitioning and implications for the geochronology of crustal rocks. Chem Geol 241(1):38–61

Rubin AE, Cooper KM, Till CB, Kent AJ, Costa F, Bose M, Gravley D, Deering C, Cole J (2017) Rapid cooling and cold storage in a silicic magma reservoir recorded in individual crystals. Science 356(6343):1154–1156

Schaltegger U (2007) Hydrothermal zircon. Elements 3(1):51–79

Shannon RD (1976) Revised effective ionic radii and systematic studies of interatomic distances in halides and chalcogenides. Acta Crystallogr Sect A 32(5):751–767

Spandler C, Hermann J, Rubatto D (2004) Exsolution of thortveitite, yttrialite, and xenotime during low-temperature recrystallization of zircon from New Caledonia, and their significance for trace element incorporation in zircon. Am Mineral 89(11–12):1795–1806

Speer J (1980) Zircon. Rev Mineral Geochem 5(1):67–112

Stelten ME, Cooper KM, Vazquez JA, Calvert AT, Glessner JJ (2015) Mechanisms and timescales of generating eruptible rhyolitic magmas at Yellowstone Caldera from zircon and sanidine geochronology and geochemistry. J Petrol 56(8):1607–1642

Stelten ME, Champion DE, Kuntz MA (2017) The timing and origin of pre-and post-caldera volcanism associated with the Mesa Falls Tuff, Yellowstone Plateau volcanic field. J Volcanol Geotherm Res 350:47–60

Szymanowski D, Wotzlaw J-F, Ellis BS, Bachmann O, Guillong M, von Quadt A (2017) Protracted near-solidus storage and pre-eruptive rejuvenation of large magma reservoirs. Nat Geosci 10(10):777

Thomas R, Webster J, Heinrich W (2000) Melt inclusions in pegmatite quartz: complete miscibility between silicate melts and hydrous fluids at low pressure. Contrib Mineral Petrol 139(4):394–401

Troch J, Ellis BS, Mark DF, Bindeman IN, Kent AJR, Guillong M, Bachmann O (2017) Rhyolite generation prior to a Yellowstone supereruption: Insights from the Island Park-Mount Jackson rhyolite series. J Petrol 0(0):1–24

Van Lichtervelde M, Melcher F, Wirth R (2009) Magmatic vs. hydrothermal origins for zircon associated with tantalum mineralization in the Tanco pegmatite, Manitoba, Canada. Am Mineral 94(4):439–450

Vazquez JA, Kyriazis SF, Reid MR, Sehler RC, Ramos FC (2009) Thermochemical evolution of young rhyolites at Yellowstone: evidence for a cooling but periodically replenished postcaldera magma reservoir. J Volcanol Geotherm Res 188(1–3):186–196. https://doi.org/10.1016/j.jvolgeores.2008.11.030

Vazquez JA, Velasco NO, Schmitt AK, Bleick HA, Stelten ME (2014) 238 U–230 Th dating of chevkinite in high-silica rhyolites from La Primavera and Yellowstone calderas. Chem Geol 390:109–118

Veksler IV, Thomas R, Schmidt C (2002) Experimental evidence of three coexisting immiscible fluids in synthetic granitic pegmatite. Am Mineral 87(5–6):775–779

Wang D, Wang X-L, Cai Y, Chen X, Zhang F-R, Zhang F-F (2017) Heterogeneous conservation of zircon xenocrysts in late jurassic granitic intrusions within the Neoproterozoic Jiuling Batholith, South China: a magma chamber growth model in deep crustal hot zones. J Petrol 58(9):1781–1810

Watson EB (1985) Henry's law behavior in simple systems and in magmas: criteria for discerning concentration-dependent partition coefficients in nature. Geochim Cosmochim Acta 49(4):917–923

Weber WJ, Ewing RC, Wang L-M (1994) The radiation-induced crystalline-to-amorphous transition in zircon. J Mater Res 9(3):688–698

Webster J, Holloway J, Hervig R (1989) Partitioning of lithophile trace elements between H_2O and $H_2O + CO_2$ fluids and topaz rhyolite melt. Econ Geol 84(1):116–134

Wiedenbeck M, Alle P, Corfu F, Griffin W, Meier M, Oberli FV, Quadt AV, Roddick J, Spiegel W (1995) Three natural zircon standards for U-Th-Pb, Lu-Hf, trace element and REE analyses. Geostand Geoanal Res 19(1):1–23

Wiedenbeck M, Hanchar JM, Peck WH, Sylvester P, Valley J, Whitehouse M, Kronz A, Morishita Y, Nasdala L, Fiebig J (2004) Further characterisation of the 91500 zircon crystal. Geostand Geoanal Res 28(1):9–39

Wotzlaw J-F, Bindeman IN, Stern RA, D'Abzac F-X, Schaltegger U (2015) Rapid heterogeneous assembly of multiple magma reservoirs prior to Yellowstone supereruptions. Sci Rep 5:14026

Yin R, Wang RC, Zhang A-C, Hu H, Zhu JC, Rao C, Zhang H (2013) Extreme fractionation from zircon to hafnon in the Koktokay No. 1 granitic pegmatite, Altai, northwestern China. Am Mineral 98(10):1714–1724

Zajacz Z, Halter WE, Pettke T, Guillong M (2008) Determination of fluid/melt partition coefficients by LA-ICPMS analysis of coexisting fluid and silicate melt inclusions: controls on element partitioning. Geochim Cosmochim Acta 72(8):2169–2197

Zeng L-J, Niu H-C, Bao Z-W, Yang W-B (2017) Chemical lattice expansion of natural zircon during the magmatic-hydrothermal evolution of A-type granite. Am Mineral 102(3):655–665

Zhang M, Salje EK, Farnan I, Graeme-Barber A, Daniel P, Ewing RC, Clark AM, Leroux H (2000) Metamictization of zircon: Raman spectroscopic study. J Phys Condens Matter 12(8):1915